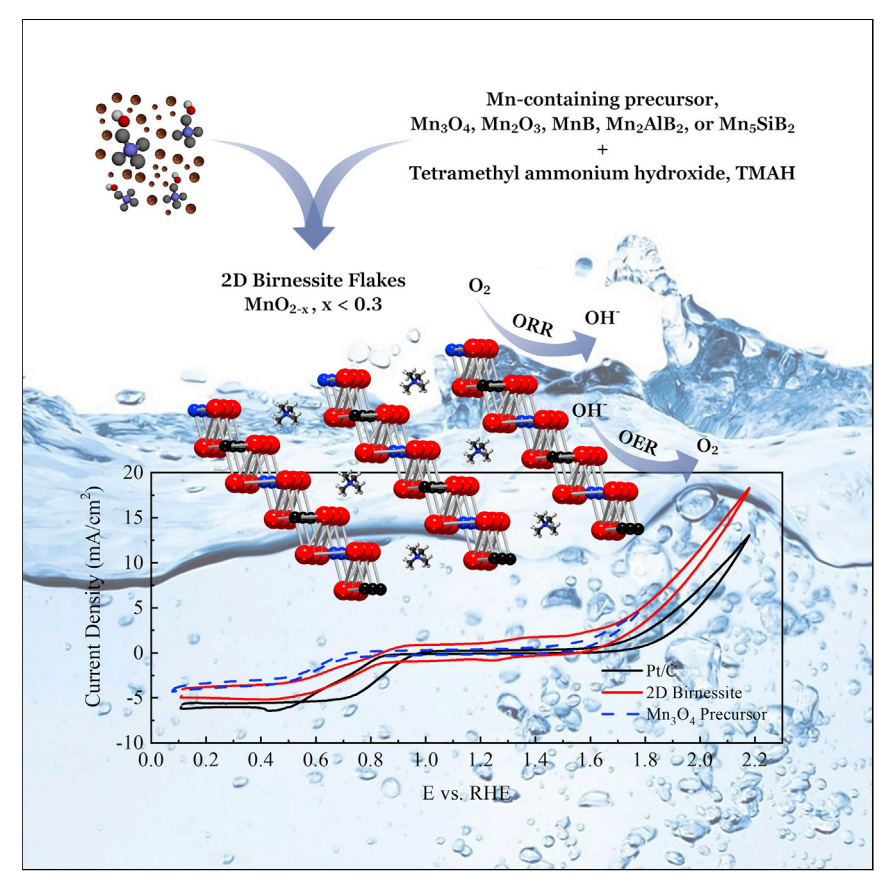
**Matter** 



## **Article**

# Scalable, inexpensive, one-pot, facile synthesis of crystalline two-dimensional birnessite flakes



Two-dimensional materials are usually prepared using special chemicals and higher temperature processes and/or using hazardous chemicals such as hydrofluoric acid. Herein, we present a near-ambient condition (50° to 80°C), nontoxic, one-pot, cheap, scalable pathway to convert five different water-insoluble, non-layered Mn-containing precursors, viz. Mn<sub>3</sub>O<sub>4</sub>, Mn<sub>2</sub>O<sub>3</sub>, MnB, Mn<sub>5</sub>SiB<sub>2</sub>, and Mn<sub>2</sub>AlB<sub>2</sub>, into 2D crystalline birnessite flakes. The resulting flakes demonstrated electrocatalytic activities for reversible O<sub>2</sub> reactions that are comparable with Pt/C electrodes.

Hussein O. Badr, Kiana Montazeri, Tarek El-Melegy, ..., Young-Jie Hu, Joshua Snyder, Michel W. Barsoum

jds43@drexel.edu (J.S.) barsoumw@drexel.edu (M.W.B.)

#### Highlights

Scalable, inexpensive, one-pot, facile synthesis of 2D birnessite flakes

Near-ambient conversion of water-insoluble, non-layered Mnprecursors

Resulting birnessite flakes are crystalline, with thicknesses around  $\approx$  2  $\pm$  0.4 nm

Reversible  $O_2$  electrocatalysis with activities comparable with those of a Pt/C catalyst



Badr et al., Matter 5, 2365–2381 July 6, 2022 © 2022 Elsevier Inc. https://doi.org/10.1016/j.matt.2022.05.038



## **Matter**



#### **Article**

## Scalable, inexpensive, one-pot, facile synthesis of crystalline two-dimensional birnessite flakes

Hussein O. Badr,<sup>1,2</sup> Kiana Montazeri,<sup>1</sup> Tarek El-Melegy,<sup>1</sup> Varun Natu,<sup>1</sup> Michael Carey,<sup>1</sup> Ramchandra Gawas,<sup>3</sup> Phu Phan,<sup>3</sup> Qian Qian,<sup>1</sup> Christopher Y. Li,<sup>1</sup> Ulf Wiedwald,<sup>4</sup> Michael Farle,<sup>4</sup> Erika Colin-Ulloa,<sup>5</sup> Lyubov V. Titova,<sup>5</sup> Marc Currie,<sup>6</sup> Thierry Ouisse,<sup>7</sup> Maxime Barbier,<sup>7,8</sup> Andrei Rogalev,<sup>8</sup> Fabrice Wilhelm,<sup>8</sup> Marcus Hans,<sup>9</sup> Jochen M. Schneider,<sup>9</sup> Christopher Tandoc,<sup>1</sup> Young-Jie Hu,<sup>1</sup> Joshua Snyder,<sup>3,\*</sup> and Michel W. Barsoum<sup>1,10,\*</sup>

#### **SUMMARY**

Synthesis of two-dimensional (2D) materials that is readily scalable, cost-effective, and eco-friendly is important from both scientific and industrial viewpoints. Currently, these 2D materials are synthesized either by selective etching of relatively expensive layered solids, viz. using a top-down approach, or by autoclaving metal salts/organic compounds. Herein, we describe a near-ambient, one-pot, inexpensive, scalable pathway to convert—through a bottom-up approach—5 different water-insoluble Mn-bearing precursors, viz. Mn<sub>3</sub>O<sub>4</sub>, Mn<sub>2</sub>O<sub>3</sub>, MnB, Mn<sub>5</sub>SiB<sub>2</sub>, and Mn<sub>2</sub>AlB<sub>2</sub>, into birnessite-based 2D flakes that, in some cases, are remarkably crystalline. The precursor powders are immersed in 25 wt % tetramethylammonium hydroxide aqueous solutions at 50°C to 80°C for 2 to 4 days. The structures, compositions, oxidation states, and morphologies of the synthesized flakes are determined using a battery of characterization techniques. The synthesized 2D sheets demonstrate reversible O<sub>2</sub> electrocatalysis with activities comparable with those of a commercial Pt/C catalyst.

#### **INTRODUCTION**

Manganese oxides with at least six different polymorphs labeled  $\alpha$ ,  $\beta$ ,  $\gamma$ ,  $\lambda$ , R, and δ-MnO<sub>x</sub><sup>1,2</sup> have been widely explored for various applications such as batteries, <sup>3,4</sup> supercapacitors, <sup>5–7</sup> heavy-metal adsorption, <sup>8,9</sup> and many more. <sup>10–12</sup> More recently, manganese oxides with a broad range of active-site configurations, nominal valence states, and nano-morphologies have been developed and tested as oxygen electrocatalysts, oxygen evolution reactions (OERs), and oxygen reduction reactions (ORRs) for some time. 13-22 What makes these materials attractive is their comparatively high activity, with respect to other non-platinum-group metals (non-PGMs), unique reversibility for oxygen electrocatalysis, and dramatically lower cost compared with other catalyst materials. 13-22 The electrocatalytic activity and reversibility have been related to the Mn<sup>2+/3+</sup>/Mn<sup>4+</sup> redox couples. 14,15,23-28 And while the specific/normalized electrocatalytic activity for MnO<sub>x</sub>-based materials remains below that of respective PGM materials, the increase in material abundance and decrease in cost more than offsets this activity disparity. This renders  $MnO_x$  nanomaterials attractive replacements for PGM catalysts when the total electrode area of an electrochemical energy conversion/storage scheme is not limiting, as in stationary power applications, for example.

#### **Progress and potential**

Typically, materials that are atomically thick but extend over large areas are labeled twodimensional (2D) materials, which are produced by exfoliating or etching layered bulk materials. The process can be slow and hazardous and can render the production of 2D materials in large quantities challenging and expensive. We developed a onepot recipe of producing 2D sheets in bulk scale almost at room temperature, starting with inexpensive green precursors. The quality of sheets produced is as high as those prepared using high temperatures and pressures and/or hazardous chemicals. Our one-pot method is thus the simpler, scalable, cheaper, and safer approach.

Electrodes made with our materials could lead to better batteries for cell phones and transportation. The sheets are also biocompatible, which renders them good candidates for use in the biomedical field. This discovery is a true breakthrough in scaling up the production of nanomaterials and will have a direct and positive impact on society.







Of special interest to this work are manganese oxide two-dimensional (2D) sheets. Layered manganese oxide—labeled  $\delta$ -MnO<sub>2</sub><sup>29</sup> or manganous manganite<sup>29–31</sup>—was first synthesized by McMurdie in 1944. A few years later, naturally occurring δ-MnO<sub>2</sub> was discovered in Canada. 32 Interestingly, it was not until 1956 when it was named birnessite after natural deposits were found in Birness, Scotland. 33 Conventionally, δ-MnO<sub>2</sub> is prepared through one of the following bottom-up pathways: reduction of KMnO<sub>4</sub>, <sup>34,35</sup> topotactic oxidation of Mn<sup>2+</sup> salts in the presence of alkali ions (i.e., in alkaline media), <sup>11,36,37</sup> or hydrothermal treatment of Mn inorganic compounds such as Mn salts or oxides<sup>38–43</sup> or a mixture of divalent Mn salts and KMnO<sub>2</sub>. 44-46 The flakes obtained using these bottomup approaches, however, are usually not monosheets. It was not until 2008 that Kai et al.<sup>47</sup> added tetramethyl ammonium hydroxide (TMAH) and hydrogen peroxide (H<sub>2</sub>O<sub>2</sub>) into aqueous solutions of manganese(II) chloride (MnCl<sub>2</sub>) and obtained colloidal suspensions of mostly MnO<sub>2</sub> monosheets.

In general, to obtain relatively large single 2D flakes of highly crystalline birnessite, the preferred synthesis approach is a top-down one in which layered manganese oxides are exfoliated using organic surfactants, such as tetramethyl ammonium (TMA+) or tetrabutyl ammonium (TBA<sup>+</sup>) cations. <sup>48–50</sup> This approach, however, is not easily scalable and is significantly more expensive and time consuming than bottom-up approaches.

Very recently, we showed that by heating 10 different water-insoluble Ti-containing solids (carbides, nitrides, borides, etc.) at near-ambient conditions, in TMAH aqueous solutions, we converted them into C-containing, anatase-based nanofilaments (nfs) that self-assemble in 2D flakes. <sup>51</sup> The nfs are  $\approx 6 \times 10 \,\text{Å}^2$  in cross-section, and some are microns long. The vast majority, however, are significantly shorter. In that case, the organic salt acted both as a near-universal solvent and a templating agent allowing growth in only one direction.

One of the purposes of this work was to test the general validity of this approach on non-Ti based materials, specifically water-insoluble Mn-containing powders, viz. Mn<sub>3</sub>O<sub>4</sub>, Mn<sub>2</sub>O<sub>3</sub>, MnB, Mn<sub>5</sub>SiB<sub>2</sub>, and Mn<sub>2</sub>AlB<sub>2</sub>. Herein, we heated powders of these compounds in 25 wt % TMAH at near-ambient conditions for 2-4 days in the 50°C-80°C temperature range and obtained crystalline, relatively large birnessitebased 2D flakes, henceforth referred as TMAH-processed birnessite or TMB. We further investigated the electrocatalytic activity of the latter for both OER and ORR.

#### **RESULTS AND DISCUSSION**

The experimental details can be found in the experimental procedures. A schematic of our synthesis approach is shown in Figure 1A. Table S1 lists all starting precursors and chemicals used. In all cases, the Mn:TMAH molar ratio was kept at 0.47. Table S2 summarizes the conditions used in 14 different reactions, all resulting in TMB. After reaction, the resulting sediment was washed with ethanol until the pH  $\approx 7$  and was redispersed in water to yield stable colloidal suspensions that were, in turn, filtered to produce highly flexible, free-standing filtered films (FFs) (Figure 1A). Figure 1B shows isometric side and top views of the 2D monoflakes produced. Typical crosssectional scanning electron microscopy (SEM) micrographs of FFs derived from Mn<sub>3</sub>O<sub>4</sub> (Figure 2A) and other precursors (Figure S1) clearly reveal the presence of well-stacked 2D layers.

Figures S2A and S2B show X-ray diffraction (XRD) patterns of FFs derived from  $Mn_3O_4$ ,  $Mn_2O_3$ , MnB, and  $Mn_2AlB_2$  powders heated in TMAH for the various times

<sup>1</sup>Department of Material Science and Engineering, Drexel University, Philadelphia, PA,

<sup>2</sup>Department of Metallurgical Engineering, Faculty of Engineering, Cairo University, Giza 12316, Egypt

<sup>3</sup>Department of Chemical & Biological Engineering, Drexel University, Philadelphia, PA,

<sup>4</sup>Faculty of Physics and Center for Nanointegration Duisburg-Essen (CENIDE), University of Duisburg-Essen, Duisburg, Germany

<sup>5</sup>Department of Physics, Worcester Polytechnic Institute, Worcester, MA, USA

<sup>6</sup>United States Naval Research Lab., Optical Sciences Division, Washington, DC, USA

<sup>7</sup>Univ. Grenoble Alpes, LMGP, 38000 Grenoble, France

<sup>8</sup>European Synchrotron Radiation Facility (ESRF), Grenoble, France

<sup>9</sup>Materials Chemistry, RWTH Aachen University, Kopernikusstr. 10, 52074 Aachen, Germany

<sup>10</sup>Lead contact

\*Correspondence: jds43@drexel.edu (J.S.), barsoumw@drexel.edu (M.W.B.)

https://doi.org/10.1016/j.matt.2022.05.038



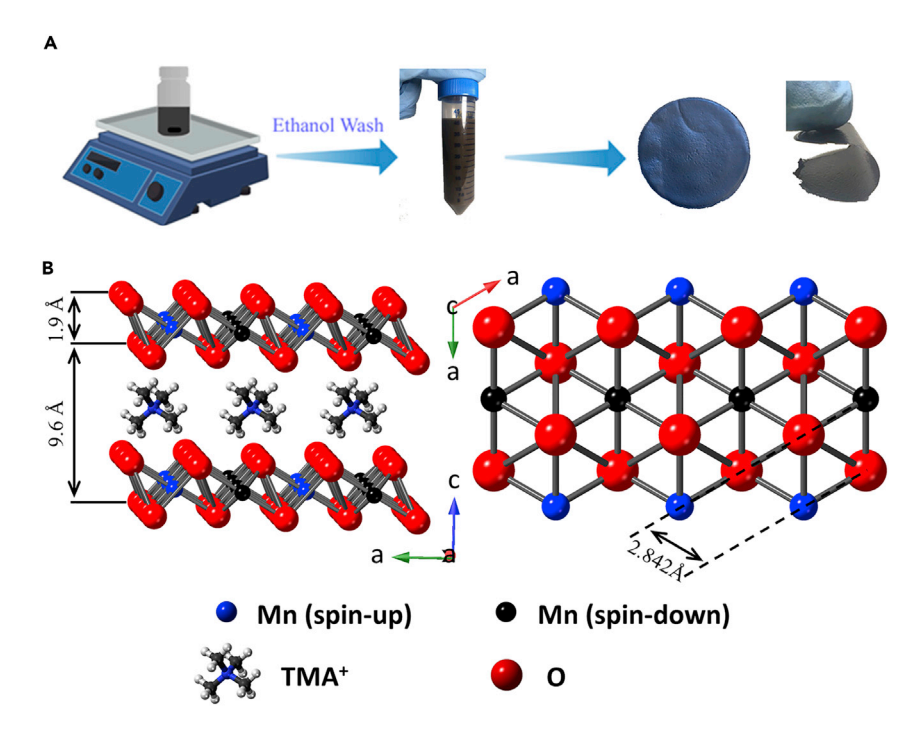


Figure 1. Schematic of processing procedure and atomic models of birnessite

(A) Schematic of fabrication process of colloidal suspensions and FFs of TMB derived from various precursors (see Tables S1 and S2).

(B) Isometric side and top views of relaxed structure of single layer of birnessite (see DFT calculations in experimental procedures). Thicknesses of manganese oxide layer and TMA molecule associated with hydration layers are 1.9 and 7.7 Å, respectively. 44 Note that arrows denote approximate dimensions and are not to scale. Corresponding axes are shown between the two schematics. Bottom axes refer to left schematic, and top axes refer to right schematic. The caxis is the stacking direction.

and temperatures indicated on the graphs. In all cases, the obtained XRD patterns were characterized by up to eight 00L reflections with a basal spacing, d, of  $\approx 9.62$  Å, a value that agrees with previous reports on TMA<sup>+</sup>-intercalated birnessite. A4,47,52–54 We note in passing that our 00L peaks are significantly more intense than those reported previously. This distance is the sum of the thickness of a single slab of MnO<sub>x</sub> octahedra of  $\approx 1.9$  Å (see below) and 7.7 Å attributed to hydrated TMA<sup>+</sup> molecules. The absence of precursor XRD peaks is noteworthy and confirms the effectiveness of our reaction and washing protocols and how well the 2D flakes are separated from the unreacted sediment.

When the XRD pattern of FFs obtained by heating  $Mn_3O_4$  in TMAH at  $80^{\circ}C$  for 4 days (Figure S2A, blue curve) is plotted on a log scale (Figure 2B), in addition to the intense 00L reflections, we also observe two less intense peaks corresponding to the (100) and (110) planes. To confirm their presence, we obtained XRD patterns, in transmission mode, of vertically aligned FFs. In such a setup, basal reflections are suppressed, and the only remaining peaks are those belonging to the (100) and (110) planes (Figure 2B, black curve) with d spacings of 2.48 and 1.44 Å, respectively. These reflections are characteristic of hexagonal birnessite and are in gratifying agreement with other reports on layered  $MnO_2$  sheets intercalated with various quaternary ammonium cations. Moreover, the asymmetric broadening of these non-basal peaks suggest that the stacked lamellas are rotated relative to each other about the c axis.  $^{54,56}$ 

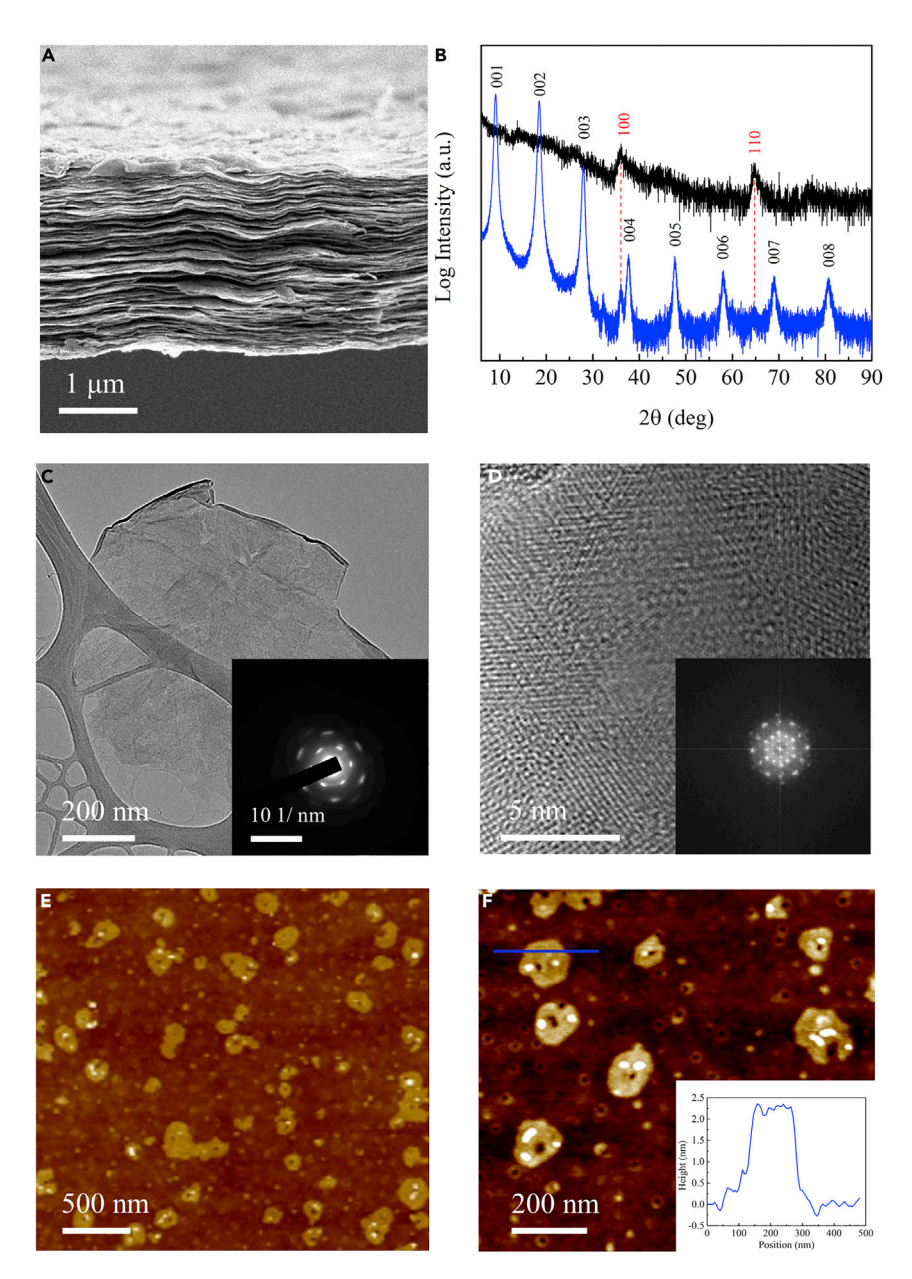


Figure 2. Characterization of TMB flakes prepared by heating Mn<sub>3</sub>O<sub>4</sub> in TMAH at 80°C for 4 days then washing with ethanol

- (A) SEM micrograph of typical FF's cross-section.
- (B) XRD patterns, on log scale, of FFs in both horizontal (blue curve) and vertical (black curve) directions. Vertical red lines indicate the  $2\theta$  locations of non-basal peaks.
- (C) Typical TEM image of TMB flake. Inset shows corresponding SAED pattern.
- (D) HRTEM of a similar 2D sheet. Inset shows corresponding FFT pattern consistent with that of birnessite. (E and F) AFM height images—at various magnifications—of TMB sheets prepared by spin coating on glass slides. Inset shows height profile corresponding to blue line in (F).

Interestingly, the thickness of a  $\mbox{MnO}_{\mbox{\scriptsize x}}$  octahedral layer reported in the literature range from 1.9 to 4.5  $\mathring{\text{A}}$   $^{44,52,54}$  To obtain a more accurate value, we carried out a density functional theory (DFT) calculation on birnessite. We predict a thickness of  $\approx$  1.9 Å and a lattice parameter of 2.842 Å. The latter agrees quite well with the 2.864 Å value deduced from the XRD patterns (Figure 2B).





Figure 2C shows a typical transmission electron microscope (TEM) image of a single TMB flake with a lateral size  $\approx 0.5~\mu m$ . The selected-area electron diffraction (SAED) of this flake depicts two sets of diffraction spots arranged in a hexagonal pattern (Figure 2C, inset) with d spacings of 2.51 and 1.48 Å that correspond to the (100) and (110) planes, respectively. The agreement between the SAED and XRD results (Figure 2B) is important and confirms that the flakes observed in the TEM are representative of our FFs' microstructure. The fact that the SAED shows spots is compelling evidence for the single-crystalline nature of the flakes imaged. However, in other regions, the SAED patterns (Figures S3B–S3F, insets) degenerated into two rings—with the same d-spacing values—suggesting a turbostratic arrangement of the 2D crystalline sheets and/or their overlap. High-resolution TEM (HRTEM) imaging (Figure 2D) verified the crystalline nature of the flakes at the atomic-layers scale. Fast Fourier transform (FFT) of the micrograph shown (Figure 2D, inset) is consistent with a highly crystallized flake. This is in excellent agreement with the SAED patterns and confirms our flakes' hexagonal structure and crystallinity.

TEM micrographs of  $Mn_3O_4$ -derived flakes treated at different processing conditions (Figure S3) show consistent morphology of 2D sheets, with lateral sizes ranging from 100–500 nm or even larger. Atomic force microscopy (AFM) height maps of a 300× diluted suspension made from  $Mn_3O_4$  powders heated at 80°C for 4 days (Figures 2E and 2F) and drop cast on glass slides reveal that the lateral sizes of the 2D sheets are closer to the 200 nm range. An AFM height profile, along the blue line in Figure 2F, shows that the flake thicknesses are  $\approx 2 \pm 0.4$  nm (Figure 2F, inset). Notably, the same height was obtained for most of the flakes shown in Figure 2F, suggesting that each cluster comprises 2–3 birnessite layers. Tellingly, some of the domains are hexagonal in shape.

Typical Raman spectra of FFs (Figure 3A) show one dominant band at  $570 \text{ cm}^{-1}$  and two less intense bands at  $490 \text{ and } 640 \text{ cm}^{-1}$ . These values agree with other reports on birnessite in the literature. <sup>1,57</sup> The  $570 \text{ cm}^{-1}$  intense peak originates from the M–O in-plane stretching vibrations and is consistent with a system where MnO<sub>6</sub> octahedra are preferentially aligned along the a and b axes. <sup>1,57</sup>

To shed light on the Mn average oxidation state, Figure 3B plots the X-ray absorption near edge structure (XANES) spectra for  $Mn_3O_4$ -derived flakes as well as those of MnO,  $Mn_2O_3$ , and  $MnO_2$  powders for comparison. Based on these results, we conclude that the Mn average oxidation state falls between +3 and +4, which is fully consistent with other XANES measurements on birnessite. S2,53,58 As discussed below, these values also agree well with those deduced from XPS.

X-ray photoelectron spectroscopy (XPS) spectra of a  $Mn_3O_4$ -derived FFs (Figure 3C) show that the binding energies (BEs) of Mn and O in the Mn 2p and O 1s regions, respectively, are comparable with those in the literature for TMA<sup>+</sup>-intercalated birnessite. When the XPS results for all TMB obtained from different precursors are compared (Figure S4), it is obvious that the Mn BEs are identical and are not a function of precursor chemistry. With one exception, viz. MnAlB (Figure S4B), the same is true of the O BEs. Fitting the various XPS peaks (see experimental procedures), we conclude the flakes' composition to be  $MnO_x$ , with  $x \approx 1.7$ –2. This range is in part attributed the uncertainty of the hydroxide content in the birnessite flakes (Figure 3C, hydroxide peak). See the simple section of the procedure of

The low BE shoulder observed around  $\sim$ 641 eV in the Mn  $2p_{3/2}$  peak (Figure S4A) can be possibly due to presence of Mn<sup>+3</sup>. However, due to the multiple-splitting effect





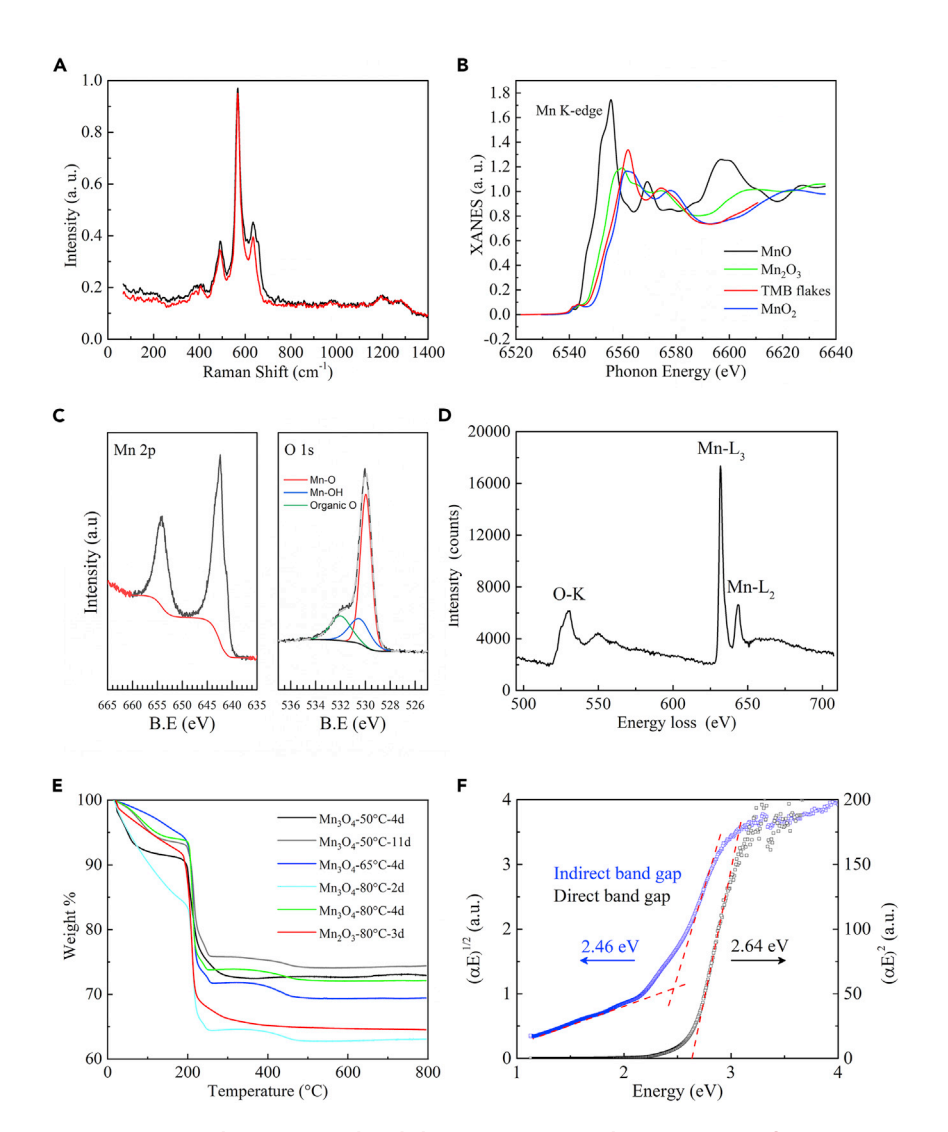


Figure 3. Structural, compositional, and electronic properties characterizations of TMB-FF produced by heating  $\rm Mn_3O_4$  in TMAH at 80°C for 4 days then washing with ethanol

- (A) Raman scattering spectra.
- (B) XANES spectra, together with those of some of related precursors—MnO, Mn<sub>2</sub>O<sub>3</sub>, and MnO<sub>2</sub>.
- (C) XPS spectra of Mn  $^2$ p and O 1s regions. Red and black lines in the Mn  $^2$ p and O 1s regions, respectively, are the backgrounds used.
- (D) Core-loss EELS data measured from a FF redispersed on a TEM grid.
- (E) Thermogravimetric plot for samples derived from  $Mn_3O_4$  and  $Mn_2O_3$  powders under various conditions as indicated. TGA furnace was ramped at  $10^{\circ}$ C/min up to  $800^{\circ}$ C under flowing Ar.
- (F) Tauc plot of TMB revealing indirect ( $\approx$  2.5 eV) and direct ( $\approx$  2.6 eV) band gaps.

observed in Mn oxides,  $^{60}$  it is not possible to quantify it using XPS alone. More work is needed to quantify the Mn<sup>+3</sup> and Mn<sup>+4</sup> contributions for birnessite obtained from different precursors, but as the Mn  $2p_{3/2}$  is centered around  $\sim\!642.5$  eV, the majority contribution must be from Mn<sup>+4</sup>.

The absence of B, Al, or Si in the XPS results (Figure S5) confirms the purity of the films and the effectiveness of our washing protocol in ridding the colloid suspension of all elements except Mn and O in addition to C. Note that the latter is advantageous.



A few films were LiCl-solution washed before subjected to atomic probe tomography (APT). APT maps of films washed with ethanol and with ethanol followed by a LiCl solution are shown in Figures S6C and S6D, respectively. This was done to assess whether ion exchange is possible. Comparing the two maps, we conclude it is possible. Furthermore, after LiCl washing, the C or N signal vanishes, confirming that they originated in the TMA and are no longer present after ion exchange.

Electron energy-loss spectroscopy (EELS) on  $Mn_3O_4$ -derived flakes (Figure 3D) yields an O:Mn ratio of 1.84  $\pm$  0.11. Based on the totality of our results, it is reasonable to conclude that the chemistry of our flakes is  $MnO_{2-x}$ , where x < 0.3.

Figure 3E shows typical thermogravimetric profiles of various synthesized TMB films performed in Ar up to  $800^{\circ}$ C. Regardless of the starting precursor and/or the synthesis conditions—delineated in the figure—up to  $200^{\circ}$ C, a gradual weight loss of  $\approx 12\% \pm 5\%$  is observed. At  $200^{\circ}$ C, a steep weight loss event of  $\approx 17\% \pm 4\%$  is observed. The first could be due to the loss of interlayer water, while the second is most likely due to the decomposition of the TMA molecules intercalating the layers. A final slight weight loss ( $\approx 2\% - 3\%$ ) was noted in the  $250^{\circ}$ C– $480^{\circ}$ C temperature range that most probably corresponds to oxygen release, due to the structural transformation from MnO<sub>2-x</sub> to Mn<sub>3</sub>O<sub>4</sub>. Indeed, a XRD pattern of an FF after thermogravimetric analysis (TGA) (Figure S7A) shows a typical pattern of Mn<sub>3</sub>O<sub>4</sub>. This result is in agreement with Ma et al., who heated Na<sup>+</sup>-intercalated birnessite (protonated/washed with HCl) in air to 1,000°C. And Moreover, the Mn oxidation state in XPS after heating to  $800^{\circ}$ C in Ar is identical to that of the precursor Mn<sub>3</sub>O<sub>4</sub> (Figure S7B).

In 1988, Cornell and Giovanoli showed that immersing Hausmannite ( $Mn_3O_4$ ) in an alkaline medium such as NaOH or KOH aqueous solutions, at temperatures between 25°C to 90°C, yielded plates/laths of birnessite. <sup>61</sup> The reaction was quite slow, requiring weeks to months to complete. The authors speculated that the process starts by the dissolution of  $Mn_3O_4$  until the solution is saturated with an Mn species, at which point birnessite precipitated directly from solution. No intermediate oxides or hydroxides were observed. It is reasonable to conclude that the same is true herein, except that now the dissolution rate is greatly enhanced by the presence of TMAH. Additionally, the TMA molecules must act as capping agents that allow the flakes to only grow in plane. The resulting product in our case is thin sheets  $\approx 2 \pm 0.4$  nm thick and not crystallites, thick plates, or nanoparticles reported by others. We note in passing that TMAH-assisted growth has been previously adopted to grow  $MnO_2$ - and  $TiO_2$ -based flakes. <sup>47,62</sup> The starting precursors in these two cases were  $MnCl_2$  and  $TiCl_4$ , respectively.

To shed light on the band structure and the films' optical properties, we measured the UV-visible optical absorption spectra in the 200–800 nm wavelength range (see Figure 3F). The Tauc constructions generated from these results show an indirect band gap ( $E_g$ ) of 2.46 eV and a closely positioned direct  $E_g$  at 2.64 eV, together with a pronounced Urbach tail presumably as a result of optical transitions between sub-gap defect states (Figure 3F). These values agree with what has been reported for birnessite structures, with slightly higher values here due to the reduced dimensionality of our TMB. Moreover, our DFT calculations predict indirect and direct band gaps around 2.0 and 2.4 eV (Figure S8A), respectively. The former is identical to that obtained by Kitchaev et al. using the same potential (SCAN) they used. This value is slightly lower than the experimental ones shown in Figure 3F. The difference could be attributed to the effects of the interlayer water and/or TMA molecules.





Before discussing the optical properties, we also carried out DFT calculations for the phonon-band structure and vibrational frequencies of our 2D structure. Figures S8B and S8C plot the dispersion curves in the first Brillouin zone and the phonon density of states, respectively. No imaginary phonon frequencies were observed, indicating that our 2D structure is dynamically stable. These results are comparable with those recently reported by Ma et al. on the dynamic stability of all 4 polymorphs of MnO<sub>2</sub> (viz.,  $\alpha$ ,  $\beta$ ,  $\gamma$ , and  $\delta$ ) using spin-polarized DFT calculations with a Hubbard U correction. In contradistinction, however, in our calculations, the exchange-correlation effects were modeled using the recently introduced SCAN meta-GGA functional, which has been proven to yield accurate predictions on both energetics and electronic structures of MnO<sub>2</sub> polymorphs without the need of applying empirically fitted Hubbard U corrections.  $^{64,67}$ 

To further explore the optical characteristics of the films, we performed spectroscopic ellipsometry on thin films—100 nm thick drop cast on Si substrates—in the 230–1,000 nm wavelength range. Ellipsometry can measure the changes in polarization of the incident light from reflected waves from the sample. The functional dependencies of the refractive index (n) and extinction coefficients (k) of a 100 nm spin-coated film on wavelength are shown in Figures S9A and S9B, respectively. The n peaks around a wavelength of 440 nm, followed by a slight drop and a relatively flat region in the visible range, where the trend agrees with previously reported data on  $\rm MnO_2$  thin films.  $^{68,69}$  The measured peak value of n occurs at 2.7 and is affected by the material's density and is independent of the film thickness. At 470 nm, n  $\approx 2.5$ .

Figures S9C and S9D plot the real ( $e_1 = n^2 - k^2$ ) and imaginary ( $e_2 = 2nk$ ) components of the dielectric function, respectively. As shown in this figure, at the edge of the bands, due to the low number of available states, photon absorption is low, and as the energy increases, the density of states reaches its maximum, which corresponds to the absorption peaks. We conclude from this experiment that the bandedge energy corresponds to the direct band gap that was calculated by the Tauc model and equals  $\approx 2.64$  eV. By this observation, the ascending trend of the optical absorption starts at 2.64 eV, interpreted as the band gap, and peaks at 3.1 eV, interpreted as the maximum density of states as shown schematically in inset.

#### **Electrocatalytic activity**

Figures 4A and 4B show the cyclic voltammograms (CVs) in Ar-purged 0.1 M KOH for commercial platinum/carbon (Pt/C) and  $Mn_3O_4$ -derived TMB films, respectively. The faradaic features associated with Mn redox are clearly visible. With cycling, the anodic Mn redox peak reduces in peak current and shifts to higher potentials, which indicates a change in stoichiometry. XPS analysis (Figure S10) indicates that the assynthesized material is nominally  $Mn^{4+}$  ( $MnO_2$ ). However, following potential cycling and once a steady-state voltametric signal is reached, the nominal oxidation state shifts to  $Mn^{2+/3+}$ , similar in proportion to that for  $Mn_3O_4$ . Once a steady-state CV is reached, after  $\approx 30$  cycles, the voltametric signal remains stable. This observation, in combination with the XPS spectra (Figure S10), confirm that the changing CVs are associated with a change in  $MnO_x$  stoichiometry or oxidation state rather than a corrosion of the catalyst material.

Figures 4C–4E show the ORR and OER activities of the prepared TMB compared with commercial Pt/C as well as those of our bulk  $Mn_3O_4$  precursor material. Carbon (XC-72) is added to both the TMB and  $Mn_3O_4$  precursor powders to ensure sufficient conductivity. The TMB shows a dramatic enhancement in ORR performance compared

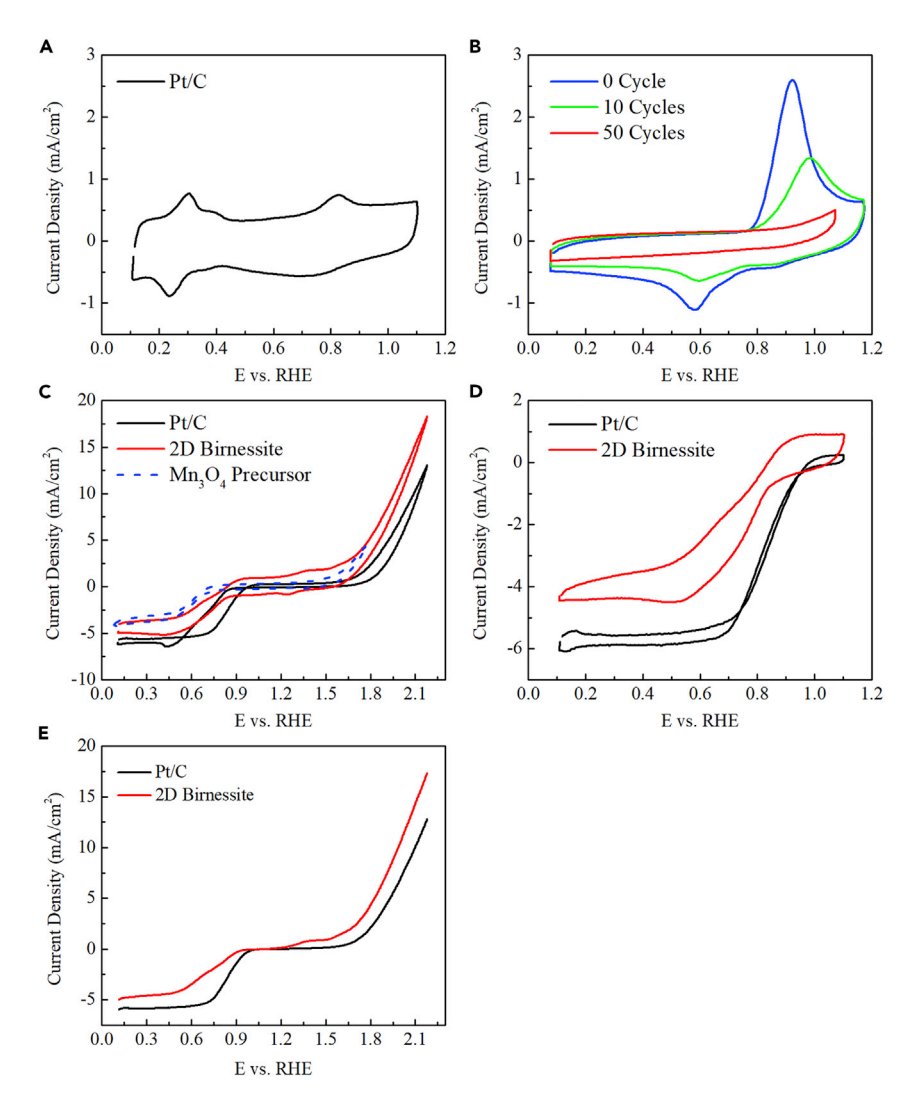


Figure 4. Electrocatalytic activity of birnessite and Pt/C

(A) CV of Pt/C in Ar-purged 0.1 M KOH.

- (B) CV of  $Mn_3O_4$ -derived flakes (80°C for 4 days) in Ar purged in 0.1 M KOH; 0 (blue), 10 (green), and 50 cycles (red).
- (C) ORR/OER polarization curves in O $_2$ -saturated 0.1 M KOH at 20 mV/s for Pt/C (black), TMB (red), and bulk Mn $_3$ O $_4$  precursor (dashed blue).
- (D) ORR polarization curves for Pt/C (black) and TMB (red) in  $O_2$ -saturated 0.1 M KOH.
- (E) Anodic sweep OER polarization curves in  $O_2$ -saturated 0.1 M KOH for Pt/C (black) and TMB (red). Potential sweep rate is 20 mV/s.

with bulk Mn $_3O_4$  precursor, approaching that of Pt/C. The observed diffusion-limited currents for the TMB indicate that the ORR is mostly through a 4-electron process. Additionally, the OER activity of the TMB significantly surpasses that observed for Pt/C, demonstrating a high degree of catalytic reversibility. The increase in ORR/OER activity for the TMB over the precursor can be attributed to its 2D morphology, yielding an increase in surface-to-volume ratio, a reduction in resistive losses per volume of material, and the bottom-up formation of a stable and active MnO $_{\rm x}$  stoichiometry.

The overall performance of our TMB for the reversible oxygen reaction is in line with previous  $MnO_x$  nanomaterials. <sup>13–22</sup> The advantage here is the ease, reproducibility,





and scalability with which our TMB flakes can be formed, greatly favoring the process and material economics. The bottom-up fabrication also leaves the door open to compositional tailoring, such as the addition of different transition metals and even multi-component oxides, and stoichiometries of the catalysts, potentially improving performance.

Lastly, it is important to distinguish this work from previous work in this field. We are not comparing our results with top-down approaches 44,45,52,70 since the latter methods are more complicated, expensive, and time consuming. Compared with previous bottom-up approaches, however, the following points are salient:

- (1) In the vast majority of previously published bottom-up approaches in this domain, the precursors were either divalent Mn salts  $^{11,36,37}$  or  $KMnO_4.^{34,35}$  Furthermore, when  $Mn^{2+}$  salts are the starting precursors, an oxidizing agent such as  $H_2O_2^{\ 71,72}$  or bubbling air or  $O_2$  is needed to yield birnessite.  $^{37,73}$  Otherwise, the reactions yield other Mn phases with reduced oxidation states, such as pyrochroite,  $Mn(OH)_2$  or  $\beta\text{-MnOOH}.^{71}$  As far as we are aware, this work is also the first where water-insoluble powders are used as a starting point.
- (2) Morphologically, by reviewing the various bottom-up protocols reported in the literature, the obtained morphologies are usually crystallites,  $^{71}$  relatively thick sheets (20 nm thick),  $^{72}$  platelets,  $^{73}$  or multilayers.  $^{74}$  It was not until 2008 that Kai et al.  $^{47}$  reported the formation of monolayer 2D flakes in a process analogous to ours. In that work, however, the starting materials were MnCl<sub>2</sub>, TMAH, and H<sub>2</sub>O<sub>2</sub>. Their AFM maps showed lateral sizes comparable to ours, viz.  $\approx$  200 nm.  $^{47}$
- (3) Typical bottom-up approaches carried out at T < 100°C under ambient pressures produce poorly crystalized birnessite flakes. To crystallize them, a higher temperature annealing step, typically hydrothermal, is needed. Herein, the flakes in some areas are single crystals. As far as we are aware, such clear SAED spots (e.g., Figures 2C and S3A) are not typical of flakes made via a bottom-up approaches. Critically, since Kai et al. did not show any TEM results, it is impossible to say anything about how well their flakes were crystallized.</p>

Lastly, starting with water-insoluble compounds greatly increases the chemical landscape allowing for doping. It is also quite likely that our overall yields are much higher than when the precursors are water-soluble salts. We are currently investigating this important aspect.

#### **Summary and conclusions**

Herein, we describe a simple, one-pot, cost-effective, fully scalable synthesis protocol that converts five water-insoluble Mn-powders—Mn $_3$ O $_4$ , Mn $_2$ O $_3$ , MnB, Mn $_2$ AlB $_2$ , or Mn $_5$ SiB $_2$ —into *crystalline* 2D hexagonal birnessite flakes. The transformation occurs by immersing the precursor powders in 25 wt % TMAH aqueous solution in the 50°C–80°C temperature range under ambient pressures for tens of hours depending on temperature. Like in our Ti-based work, <sup>51</sup> the TMAH plays a dual role: universal solvent and templating agent. This procedure results in multilayered flakes that are highly ordered in the stacking direction. From XRD patterns, an interlayer distance of 9.6 Å is calculated. This distance is the sum of the thickness of a single birnessite layer, estimated from DFT to be  $\approx$  1.9 Å, intercalated with TMA cations and water. The a-lattice parameter obtained experimentally, 2.864 Å, is also in excellent agreement with our DFT calculations of 2.842 Å. Furthermore, the calculated





phonon-dispersion curves in our DFT work demonstrate that 2D birnessite is dynamically stable.

AFM maps reveal that this process produces thin flakes  $\approx 2 \pm 0.4$  nm thick and  $\approx 200$  nm across. SAED of TEM micrographs confirm the hexagonal symmetry and crystallinity of our flakes. From XPS, XANES, and EELS, we conclude that the chemistry of our flakes is MnO<sub>2-x</sub>, where x  $\approx 0$ –0.3. APT maps verified the capability of ion exchange and the chemistry of the intercalants before and after washing with LiCl solution.

While bulk  $MnO_x$  materials are inexpensive, the challenges associated with their reproducible conversion into active nanomaterials, at scale, goes a long way to reduce their cost advantage. As bulk  $MnO_x$  materials are characterized by relatively high resistivities, it is critical to reduce their nominal length scale to mitigate resistive losses in catalytic electrodes. Additionally, high surface-to-volume ratios are required to obtain sufficient turnover numbers per mass of active material. These combined material characteristics for our birnessite yield electrocatalytic activity for the reversible  $O_2$  reaction commensurate with other  $MnO_x$  nanomaterials and rivaling that of commercial Pt/C but using a much simpler and scalable approach. Lastly, it is worth noting that in recent work, we showed that birnessite fabricated using our method functions quite well as the positive electrode in an asymmetric aqueous supercapacitor with high energy density. The second state of the property of the positive electrode in an asymmetric aqueous supercapacitor with high energy density.

#### **EXPERIMENTAL PROCEDURES**

#### Resource availability

#### Lead contact

Further information and requests for resources and reagents should be directed to and will be fulfilled by the lead contact, Michel W. Barsoum (barsoumw@drexel.edu).

#### Materials availability

This study did not generate new unique reagents.

#### Data and code availability

This study did not generate datasets and code.

#### Materials synthesis and processing

Table S1 lists all the starting precursors and the reagents used in this work. Table S2 summarizes the synthesis conditions of all 14 runs conducted. In a typical synthesis protocol, the solid precursor powder is simply immersed—at ambient conditions—in a TMAH solution and stirred mildly in the  $50^{\circ}\text{C}-80^{\circ}\text{C}$  temperature range for 2–4 days (see Table S2). The Mn:TMA molar ratio was kept constant at 0.47. The produced sediment is rinsed with ethanol until the pH  $\approx$ 7 and is redispersed in deionized (DI) water (18.2 M $\Omega$ ) to yield a stable colloidal suspension without stirring, sonication, or any other processing steps. The suspension is lastly filtered to produce highly flexible, free-standing FFs. The focus of this work is mostly on flakes derived from Mn<sub>3</sub>O<sub>4</sub> treated in TMAH at 80°C for 4 days then washed with ethanol. That being said, both Mn<sub>3</sub>O<sub>4</sub> and Mn<sub>2</sub>O<sub>3</sub> are the cheapest among all precursors.

To assess the capability of ion exchange, an additional step of washing with a LiCl solution was conducted, and the produced flakes were characterized using APT. A 5 M LiCl solution was added to the colloidal suspension obtained above. This resulted in deflocculation. The sediment was shaken and rinsed with DI water through centrifugation at 5,000 RPM for three cycles. The LiCl/DI-water washing process was repeated until the pH was  $\approx$ 7. The resulting suspension was then vacuum filtered.





#### **XRD**

A Rigaku SmartLab diffractometer operated with Cu K $\alpha$  radiation was used in the Bragg-Brentano geometry to acquire XRD patterns of vacuum-dehydrated FFs. The films were scanned in the 2°-65° 2 $\theta$  range, using a 0.02° step size and a dwell time of 1 s/step. Some samples were further characterized in the 2°-90° 2 $\theta$  range. We also obtained XRD patterns, in transmission mode, on vertically oriented films.  $^{51,55}$ 

#### **XANES**

The XANES spectra are recorded at the ESRF beamline ID12 using total fluorescence-yield detection mode in a back-scattering geometry. The experimentally measured spectra are corrected for re-absorption effects and normalized to unity for the sake of comparison.

#### Raman spectroscopy

Raman scattering spectra of FFs were collected at 300 K in air. The samples were excited with a 0.7-mW, 532-nm laser focused to a diameter of ~0.5  $\mu$ m. Scattered light was collected in the back-scattering geometry and was dispersed and detected using a high-resolution spectrograph equipped with a charge-coupled detector array (Andor SR-500i, iKon-M).

#### **XPS**

A VersaProbe 5,000 (Physical Electronics, Chanhassen, MN, USA) instrument was used to obtain XPS spectra. Each sample was analyzed before and after Ar $^+$  sputtering. The sputterings were carried out using a 3 kV Ar $^+$  ion beam for 120 s. Monochromatic Al-K $\alpha$ X-rays with a pass energy of 23.5 eV, a step size of 0.5 eV, and a spot size of 200  $\mu m$  was used to irradiate the sample surface. Samples were mounted on the XPS stage using carbon tape. CasaXPS v.2.3.19PR1.0 software was used for peak fitting and chemical-composition analysis. The obtained spectra were calibrated by setting the C–C peak to 285.0 eV.

To determine the chemical composition, the global elemental ratios were first calculated by considering the total area under the Mn 2p peaks and only the Mn-O peaks and Mn-OH components of the O 1s peaks, as given by the red and blue peaks in Figure 3C, respectively, and their corresponding relative-sensitivity factors.

#### **SEM**

Micrographs were obtained using an SEM (Zeiss Supra 50 VP, Carl Zeiss SMT AG, Oberkochen, Germany). The settings were set to an inlens detector, a 30  $\mu$ m aperture, and an accelerating voltage of 3 kV.

#### **TEM**

TEM imaging and electron-diffraction patterns were collected using a JEOL JEM2100F field-emission TEM. The TEM was operated at 200 keV and had an image resolution of 0.2 nm. Images and diffraction patterns were collected on a Gatan USC1000 CCD camera. Samples were prepared by first diluting the colloidal suspension then drop casting a few drops on a carbon-coated, lacey-carbon, copper TEM grid.

#### **HRTEM and EELS**

Images were acquired with a JEOL 2200FS TEM at an acceleration voltage of 200 kV using a 2,000  $\times$  2,000 GATAN UltraScan1000XP CCD camera. For sample preparation, a small amount of the sample powder was redispersed in ethanol. After a short sonication, 5  $\mu L$  were drop cast onto a lacey-carbon grid and dried in air. The EELS spectra were recorded in imaging mode. The core edges were extracted from the background signal using a power law.



#### **AFM**

Thicknesses of TMB flakes were obtained with an AFM (Multimode 8 AFM, Bruker Nano Surfaces). A peak-force tapping AFM imaging mode was applied to acquire the surface morphology and height profiles. The scanning was conducted with ScanAsyst-Air Silicon Nitride Probes at a scan rate of 0.6 Hz. Topographic images were recorded as the resolution of  $256 \times 256$  pixels and analyzed by Nano Scope Analysis software.

#### **APT**

Local chemical-composition analysis of  $\rm Mn_3O_4$ -derived birnessite flakes was done by laser-assisted APT using a CAMECA LEAP 4000X HR. Field evaporation was employed at 30 and 50 pJ laser pulse energy as well as 0.25% and 0.5% detection rate for TMA $^+$ - and Li $^+$ -intercalated samples, respectively. A laser pulse frequency of 125 kHz and a base temperature of 30 K were used for both sets of samples, and approximately 1 million ions were collected. IVAS 3.8.6 was used for reconstruction of atomic positions. Needle-shape atom-probe specimens were prepared by focused ion beam (FIB) according to a standard protocol.  $^{75}$ 

#### **TGA**

A thermobalance (TA Instruments Q50, New Castle, DE, USA) was used for TGA. Small pieces of FFs ( $\approx$  20 mg) were heated in sapphire crucibles at 10°C/min, under purging Ar at 10 mL/min, to 800°C.

#### **Optical properties**

UV-vis spectra were recorded using a spectrophotometer (Evolution 300 UV-Visible, Thermo Scientific). Measurements were performed in transmission mode on 1–10  $\mu$ m thick films coated onto quartz slides.

#### **DFT** calculations

DFT calculations were performed using the Vienna Ab initio simulation package (VASP)<sup>76</sup> with projector-augmented wave (PAW) pseudopotentials.<sup>77</sup> The electronic configurations of the pseudopotentials were O:[He]2s<sup>2</sup>2p<sup>4</sup> and Mn:[Ar]3p<sup>6</sup>3d<sup>5</sup>4s<sup>2</sup>. The exchange-correlation effects were modeled by employing the recently introduced SCAN meta-GGA functional, 66 which has been proven to yield accurate prediction on both energetics and electronic structures of MnO<sub>2</sub> polymorphs without the need to apply empirically fitted Hubbard U corrections. 64,67 The energy cutoff of the plane wave basis was 600 eV. The integration in the first Brillouin zone was performed with the Gaussian smearing method with a smearing width of 0.05 eV. A slab model was adopted to construct the calculation supercell to simulate a single-layer structure of birnessite. A vacuum region of 20 Å was added along the normal direction of the atomic slab to eliminate interactions between periodic images perpendicular to the slabs. Co-linear spin alignment was applied to capture the antiferromagnetic configuration of the Mn sub-lattice. A 6-atom orthorhombic unit cell was used for the structural relaxation and electronic structure calculations. A 15 × 9 × 1 meshing was applied for the k-point sampling of the first Brillouin zone. For phonon calculations, a  $4 \times 9 \times 1$  supercell was used with a k-point meshing of  $3 \times 3 \times 1$ .

#### **Electrocatalysis**

#### Cell, electrolyte, and electrode preparation

All electrochemical experiments were carried out in a fluorinated ethylene propylene (FEP) cell. Prior to its use, the FEP cell was soaked in 50% HNO $_3$ /50% H $_2$ SO $_4$  for 2 h followed by repeated boiling and rinsing with Millipore water. Alkaline electrolyte solutions were prepared using KOH pellets (99.99%, metal basis, Sigma) with Millipore water (18.2 M $\Omega$ -cm, <3 ppb TOC). The electrolyte concentration was confirmed with a pH probe.





Catalytic thin films were prepared on freshly cleaned glassy carbon disks (Sigradur G HTW) by drop casting from an ink made from the Mn suspension (conc 1 mg/mL), XC-72R carbon (1:1 ratio with Mn MOC), and a solvent that was 1:1 v/v IPA: $H_2O$ . One  $\mu L$  of Nafion solution (5 wt % ion power) was added in a 1 mL of catalyst ink to aid the dispersion. Twenty  $\mu L$  of the catalyst ink was drop cast onto the glassy carbon disk and dried under flowing Ar to achieve a 0.1 mg/cm<sup>2</sup> catalyst loading on glassy carbon.

Pt/C thin films were prepared by drop casting 14.7  $\mu$ L of the catalyst ink (1 mg/mL Pt on Vulcan carbon obtained from General Motors in 4:1 v:v H<sub>2</sub>O:IPA, 1  $\mu$ L Nafion, 5 wt %) on glassy carbon disk to achieve 15  $\mu$ g/cm<sup>2</sup> Pt loading. Glassy carbon disks were polished by 1  $\mu$ m alumina micropolish (Buehler) followed by thorough rinsing with DI water.

#### SUPPLEMENTAL INFORMATION

Supplemental information can be found online at https://doi.org/10.1016/j.matt. 2022.05.038.

#### **ACKNOWLEDGMENTS**

We acknowledge Materials Characterization Core at Drexel University, where most of the characterizations of XRD, XPS, SEM, and TEM analyses were performed. This work was funded by the Ceramics Division of NSF (1740795) and Murata Manufacturing, Co., Ltd of Japan. The WPI team acknowledges support from WPI TRIAD Seed Grant. This work was also in part funded by the Deutsche Forschungsgemeinschaft within CRC/TRR 270, project B02 (project ID 405553726). Support by the Interdisciplinary Center for Analytics on the Nanoscale of the University of Duisburg-Essen (DFG RI sources reference: RI\_00313), a DFG-funded core facility (project nos. 233512597 and 324659309), is gratefully acknowledged. We thank Hanna Pazniak and Markus Heidelmann for assistance in TEM-based imaging and spectroscopy. M.C. acknowledges support by core programs at the U.S. Naval Research Laboratory funded by the Office of Naval Research.

#### **AUTHOR CONTRIBUTIONS**

H.O.B. and M.W.B. conceived the idea and designed the experiments. H.O.B. and M.W.B. wrote the manuscript. H.O.B. and K.M. carried out synthesis. H.O.B. carried out most of the XRD, SEM, and TEM characterizations. H.O.B. and T.E.-M. carried out synthesis of boride samples. T.E.-M. carried out the vertical XRD characterization and SEM imaging of boride samples. M. Carey carried out the TGA measurements and analysis. V.N. carried out XPS measurements and analysis. M. Currie carried out the Raman measurements and analysis. M.H. and J.M.S. carried out APT measurements. R.G., P.P., and J.S. carried out the electrocatalysis work and analysis. U.W. and M.F. carried out HRTEM and EELS analyses. Q.Q. and C.Y.L. carried out AFM. T.O., M.B., A.R., and F.W. carried out the XANES measurements. C.T. and Y.-J.H. carried out DFT calculations and analysis. M.W.B. supervised the project. All authors discussed the results and commented on the manuscript.

#### **DECLARATION OF INTERESTS**

There are no competing interests.

Received: May 4, 2022 Revised: May 13, 2022 Accepted: May 19, 2022 Published: June 14, 2022



#### **REFERENCES**

- Julien, C.M., Massot, M., and Poinsignon, C. (2004). Lattice vibrations of manganese oxides Part I. Periodic structures. SAA 60, 689–700. https://doi.org/10.1016/S1386-1425(03)00279-8.
- Feng, Q., Kanoh, H., and Ooi, K. (1999). Manganese oxide porous crystals. J. Mater. Chem. 9, 319–333. https://doi.org/10.1039/ a805349c
- Thackeray, M.M., et al. (1997). Manganese oxides for lithium batteries. Prog. Solid. State Ch. 25, 1–71. https://doi.org/10.1016/s0079-6786(97)81003-5.
- Thackeray, M.M., Johnson, C.S., Vaughey, J.T., Ha, N., and Hackney, S.A. (2005). Advances in manganese-oxide 'composite' electrodes for lithium-ion batteries. J. Mater. Chem. 15, 2257– 2267. https://doi.org/10.1039/B417616M.
- Boyd, S., Ganeshan, K., Tsai, W.Y., Wu, T., Saeed, S., Jiang, D., Balke, N., van Duin, A.C.T., and Augustyn, V. (2021). Effects of interlayer confinement and hydration on capacitive charge storage in birnessite. Nat. Mater. 20, 1689–1694. https://doi.org/10.1038/s41563-021-01066-4.
- Zheng, W., Halim, J., Sun, Z., Rosen, J., and Barsoum, M.W. (2021). MXene—manganese oxides aqueous asymmetric supercapacitors with high mass loadings, high cell voltages and slow self-discharge. Energy Storage Mater. 38, 438–446. https://doi.org/10.1016/j.ensm.2021. 03.011
- Wei, W., Cui, X., Chen, W., and Ivey, D.G. (2011). Manganese oxide-based materials as electrochemical supercapacitor electrodes. Chem. Soc. Rev. 40, 1697–1721. https://doi. org/10.1039/c0cs00127a.
- Manning, B.A., Fendorf, S.E., Bostick, B., and Suarez, D.L. (2002). Arsenic(III) oxidation and arsenic(V) adsorption reactions on synthetic birnessite. Environ. Sci. Technol. 36, 976–981. https://doi.org/10.1021/es0110170.
- Beak, D.G., Basta, N.T., Scheckel, K.G., and Traina, S.J. (2008). Linking solid phase speciation of Pb sequestered to birnessite to oral Pb bioaccessibility: implications for soil remediation. Environ. Sci. Technol. 42, 779–785. https://doi.org/10.1021/es071733n.
- Raymundo-Piñero, E., Khomenko, V., Frackowiak, E., and Béguin, F. (2005). Performance of manganese oxide/CNTs composites as electrode materials for electrochemical capacitors. J. Electrochem. Soc. 152, A229. https://doi.org/10.1149/1.1834913.
- Tian, Z.-R., Tong, W., Wang, J.Y., Duan, N.G., Krishnan, V.V., and Suib, S.L. (1997).
   Manganese oxide mesoporous structures: mixed-valent Semiconducting catalysts.
   Science 276, 926–930. https://doi.org/10.1126/ science.276.5314.926.
- Ding, B., Zheng, P., Ma, P., and Lin, J. (2020). Manganese oxide nanomaterials: synthesis, properties, and theranostic applications. Adv. Mater. 32, 1905823. https://doi.org/10.1002/ adma.201905823.
- 13. Zhong, Y., Dai, J., Xu, X., Su, C., and Shao, Z. (2020). Facilitating oxygen redox on

- manganese oxide nanosheets by tuning active species and oxygen defects for zinc-air batteries. Chemelectrochem 7, 4949–4955. https://doi.org/10.1002/celc.202001419.
- Su, H.-Y., Gorlin, Y., Man, I.C., Calle-Vallejo, F., Norskov, J.K., Jaramillo, T.F., and Rossmeisl, J. (2012). Identifying active surface phases for metal oxide electrocatalysts: a study of manganese oxide bi-functional catalysts for oxygen reduction and water oxidation catalysis. Phys. Chem. Chem. Phys. 14, 14010– 14022. https://doi.org/10.1039/c2cp40841d.
- Gorlin, Y., Lassalle-Kaiser, B., Benck, J.D., Gul, S., Webb, S.M., Yachandra, V.K., Yano, J., and Jaramillo, T.F. (2013). In situ X-ray absorption spectroscopy investigation of a bifunctional manganese oxide catalyst with high activity for electrochemical water oxidation and oxygen reduction. J. Am. Chem. Soc. 135, 8525–8534. https://doi.org/10.1021/ja3104632.
- Li, Z., Yang, Y., Relefors, A., Kong, X., Siso, G.M., Wickman, B., Kiros, Y., and Soroka, I.L. (2021). Tuning morphology, composition and oxygen reduction reaction (ORR) catalytic performance of manganese oxide particles fabricated by y-radiation induced synthesis. J. Colloid Interface Sci. 583, 71–79. https://doi. org/10.1016/j.jcis.2020.09.011.
- Stoerzinger, K.A., Risch, M., Han, B., and Shao-Horn, Y. (2015). Recent insights into manganese oxides in catalyzing oxygen reduction kinetics. ACS Catal. 5, 6021–6031. https://doi.org/10.1021/acscatal.5b01444.
- Zhang, T., Tham, N.N., Liu, Z., Fisher, A., and Lee, J.Y. (2018). Promotion of the bifunctional electrocatalytic oxygen activity of manganese oxides with dual-affinity phosphate. Electrochim. Acta 277, 143–150. https://doi. org/10.1016/j.electacta.2018.05.009.
- Gorlin, Y., and Jaramillo, T.F. (2010). A bifunctional nonprecious metal catalyst for oxygen reduction and water oxidation. J. Am. Chem. Soc. 132, 13612–13614. https://doi.org/ 10.1021/ja104587v.
- 20. Meng, Y., Song, W., Huang, H., Ren, Z., Chen, S.Y., and Suib, S.L. (2014). Structure-property relationship of bifunctional MnO<sub>2</sub> nanostructures: highly efficient, ultra-stable electrochemical water oxidation and oxygen reduction reaction catalysts identified in alkaline media. J. Am. Chem. Soc. 136, 11452–11464. https://doi.org/10.1021/ja505186m.
- Valim, R.B., Santos, M., Lanza, M., Machado, S., Lima, F., and Calegaro, M. (2012). Oxygen reduction reaction catalyzed by e-MnO<sub>2</sub>: influence of the crystalline structure on the reaction mechanism. Electrochim. Acta 85, 423–431. https://doi.org/10.1016/j.electacta. 2012.08.075.
- 22. Shi, C., Zang, G.L., Zhang, Z., Sheng, G.P., Huang, Y.X., Zhao, G.X., Wang, X.K., and Yu, H.Q. (2014). Synthesis of layered MnO<sub>2</sub> nanosheets for enhanced oxygen reduction reaction catalytic activity. Electrochim. Acta 132, 239–243. https://doi.org/10.1016/j.electacta. 2014.03.150.
- 23. Ryabova, A.S., Napolskiy, F.S., Poux, T., Istomin, S.Y., Bonnefont, A., Antipin, D.M., Baranchikov, A.Y., Levin, E.E., Abakumov, A.M.,

- Kerangueven, G., et al. (2016). Rationalizing the influence of the Mn(IV)/Mn(III) red-ox transition on the electrocatalytic activity of manganese oxides in the oxygen reduction reaction. Electrochim. Acta 187, 161–172. https://doi.org/10.1016/j.electacta.2015.11.012.
- 24. He, S., Ji, D., Novello, P., Li, X., and Liu, J. (2018). Partial surface oxidation of manganese oxides as an effective treatment to improve their activity in electrochemical oxygen reduction reaction. J. Phys. Chem. C 122, 21366–21374. https://doi.org/10.1021/acs.jpcc.8b04977.
- Nikitina, V.A., Kurilovich, A.A., Bonnefont, A., Ryabova, A.S., Nazmutdinov, R.R., Savinova, E.R., and Tsirlina, G.A. (2018). ORR on simple manganese oxides: molecular-level factors determining reaction mechanisms and electrocatalytic activity. J. Electrochem. Soc. 165, J3199–J3208. https://doi.org/10.1149/2. 0261815jes.
- Tang, Q., Jiang, L., Liu, J., Wang, S., and Sun, G. (2014). Effect of surface manganese valence of manganese oxides on the activity of the oxygen reduction reaction in alkaline media. ACS Catal. 4, 457–463. https://doi.org/10. 1021/cs400938s.
- Risch, M., Stoerzinger, K.A., Han, B., Regier, T.Z., Peak, D., Sayed, S.Y., Wei, C., Xu, Z., and Shao-Horn, Y. (2017). Redox processes of manganese oxide in catalyzing oxygen evolution and reduction: an in situ Soft X-ray absorption spectroscopy study. J. Phys. Chem. C 121, 17682–17692. https://doi.org/10.1021/ acs.jpcc.7b05592.
- Stoerzinger, K.A., Risch, M., Suntivich, J., Lu, W.M., Zhou, J., Biegalski, M.D., Christen, H.M., Ariando, Venkatesan, T., and Shao-Horn, Y. (2013). Oxygen electrocatalysis on (001)-oriented manganese perovskite films: Mn valency and charge transfer at the nanoscale. Energy Environ. Sci. 6, 1582–1588. https://doi.org/10.1039/c3ee40321a.
- Cole, W.F., Wadsley, A.D., and Walkley, A. (1947). An X-ray diffraction study of manganese dioxide. Trans. Electrochem. Soc. 92, 133. https://doi.org/10.1149/1.3071811.
- Feitknecht, W., and Marti, W. (1945). Über die Oxydation von Mangan(II)-hydroxyd mit molekularem Sauerstoff. Hel. Chern. Acta 28, 129–148. https://doi.org/10.1002/hlca. 19450280113.
- Buser, W., Graf, P., and Feitknecht, W. (1954). Beitrag zur Kenntnis der Mangan(II)-manganite und des d-MnO<sub>2</sub>. Holy. Chim. Aeta 37, 2322– 2333. https://doi.org/10.1002/hlca. 19540370746.
- McMurdie, H.F., and Golovato, E. (1948). Study
  of the modifications of manganese dioxide.
   J. Res. Natl. Bur. Stand. 41, 589–600. https://doi.org/10.6028/jres.041.046.
- Jones, L.H.P., and Milne, A.A. (1956). Birnessite, a new manganese oxide mineral from Aberdeenshire, Scotland. J. Mineral Mag. 31, 283–288. https://doi.org/10.1180/minmag. 1956.031.235.01.
- McMurdie, H.F. (1944). Microscopic and diffraction Studies on dry cells and their raw





- materials. Trans. Electrochem. Soc. 86, 313. https://doi.org/10.1149/1.3071621.
- Liu, J., Yu, L., Hu, E., Guiton, B.S., Yang, X.Q., and Page, K. (2018). Large-scale synthesis and comprehensive structure study of δ-MnO<sub>2</sub>. Inorg. Chem. 57, 6873–6882. https://doi.org/ 10.1021/acs.inorgchem.8b00461.
- Feitknecht, W., and Marti, W. (1945). Über Manganite und künstlichen Braunstein. Helv. Chim. Acta 28, 149–156. https://doi.org/10. 1002/hlca.19450280114.
- Giovanoli, R., Stähli, E., and Feitknecht, W. (1970). Über Oxidhydroxide des vierwertigen Mangans mit Schichtengitter. J. Mitteilung. Natriummangan (II, III)manganat(IV). Hel. Chern. Acta 53, 209–220. https://doi.org/10. 1002/hlca.19700530203.
- Hirano, S.i., Narita, R., and Naka, S. (1984). Hydrothermal synthesis and properties of Na<sub>0.70</sub>MnO2. 25 layer crystal. Mat. Res. Bull. 19, 1229–1235. https://doi.org/10.1016/0025-5408(84)90076-X.
- Morales, J., Navas, J.J., and Tirado, J.L. (1990). Low-temperature hydrothermal formation and ion exchange of hydrated sodium manganates. Solid State Ion 44, 125–130. https://doi.org/10. 1016/0167-2738(90)90053-t.
- Feng, Q., Kanoh, H., Miyai, Y., and Ooi, K. (1995). Hydrothermal synthesis of lithium and sodium manganese oxides and their metal ion extraction/insertion reactions. Chem. Mater. 7, 1226–1232. https://doi.org/10.1021/ cm00054a024.
- Feng, Q., Yamasaki, N., Yanagisawa, K., and Ooi, K. (1996). Hydrothermal synthesis and metal ion adsorptive property of birnessite type potassium manganese oxide. J. Mater. Sci. Lett. 15, 963–965. https://doi.org/10.1007/ bf00241438.
- Yang, X., Tang, W., Feng, Q., and Ooi, K. (2003). Single crystal growth of birnessite- and hollandite-type manganese oxides by a flux method. Cryst. Growth Des. 3, 409–415. https://doi.org/10.1021/cg0255873.
- Ma, R., Bando, Y., Zhang, L., and Sasaki, T. (2004). Layered MnO<sub>2</sub> nanobelts: hydrothermal synthesis and electrochemical measurements. Adv. Mater. 16, 918–922. https://doi.org/10. 1002/adma.200306592.
- Zhao, R., Zhang, L., Wang, C., and Yin, L. (2017). Tetramethyl ammonium cation intercalated layered birnessite manganese dioxide for highperformance intercalation pseudocapacitor.
   J. Power Sources 353, 77–84. https://doi.org/ 10.1016/j.jpowsour.2017.03.138.
- Liu, Z., Ma, R., Ebina, Y., Takada, K., and Sasaki, T. (2007). Synthesis and delamination of layered manganese oxide nanobelts. Chem. Mater. 19, 6504–6512. https://doi.org/10.1021/ cm7019203.
- Zhang, H.T., Chen, X.H., Zhang, J.H., Wang, G.Y., Zhang, S.Y., Long, Y.Z., Chenb, Z.J., and Wang, N.L. (2005). Synthesis and characterization of one-dimensional K<sub>0.27</sub>MnO<sub>2</sub>.0.5H<sub>2</sub>O. J. Cryst. Growth 280, 292–299. https://doi.org/10.1016/j.jcrysgro. 2005.02.063.
- 47. Kai, K., Yoshida, Y., Kageyama, H., Saito, G., Ishigaki, T., Furukawa, Y., and Kawamata, J.

- (2008). Room-temperature synthesis of manganese oxide monosheets. J. Am. Chem. Soc. 130, 15938–15943. https://doi.org/10. 1021/ja804503f.
- Osada, M., and Sasaki, T. (2012). Twodimensional dielectric nanosheets: novel nanoelectronics from nanocrystal Building Blocks. Adv. Mater. 24, 210–228. https://doi. org/10.1002/adma.201103241.
- Schaak, R.E., and Mallouk, T.E. (2002). Perovskites by design: a toolbox of solid-state reactions. Chem. Mater. 14, 1455–1471. https://doi.org/10.1021/cm010689m.
- Omomo, Y., Sasaki, T., Wang, L., and Watanabe, M. (2003). Redoxable nanosheet crystallites of MnO<sub>2</sub> derived via delamination of a layered manganese oxide. J. Am. Chem. Soc. 34, 3568–3575. https://doi.org/10.1002/chin. 200324215.
- Badr, H.O., El-Melegy, T., Carey, M., Natu, V., Hassig, M.Q., Johnson, C., Qian, Q., Li, C.Y., Kushnir, K., Colin-Ulloa, E., et al. (2022). Bottom-up, scalable synthesis of anatase nanofilament-based two-dimensional titanium carbo-oxide flakes. Mater. Today 54, 8–17. https://doi.org/10.1016/j.mattod.2021.10.033.
- Liu, Z.h., Ooi, K., Kanoh, H., Tang, W.p., and Tomida, T. (2000). Swelling and delamination Behaviors of birnessite-type manganese oxide by intercalation of tetraalkylammonium ions. Langmuir 16, 4154–4164. https://doi.org/10. 1021/la9913755
- Yang, X., Makita, Y., Liu, Z.h., Sakane, K., and Ooi, K. (2004). Structural characterization of self-assembled MnO<sub>2</sub> nanosheets from birnessite manganese oxide single crystals. Chem. Mater. 16, 5581–5588. https://doi.org/ 10.1021/cm049025d.
- 54. Brock, S.L., Sanabria, M., Suib, S.L., Urban, V., Thiyagarajan, P., and Potter, D.I. (1999). Particle size control and self-assembly processes in novel colloids of nanocrystalline manganese oxide. J. Phys. Chem. B 103, 7416–7428. https://doi.org/10.1021/jp991009u.
- 55. Ghidiu, M., and Barsoum, M.W. (2017). The {110} Reflection in X-ray diffraction of MXene films: misinterpretation in regards to turbostratic disorder and measurement via non-standard sample orientation. J. Amer. Ceram. Soc. 100, 5395–5399.
- Drits, V.A., et al. (1997). Structure of synthetic monoclinic Na-rich birnessite and hexagonal birnessite; I, Results from X-ray diffraction and selected-area electron diffraction. Am. Min. 82, 946–961. https://doi.org/10.2138/am-1997-9-1012
- Julien, C., Massot, M., Baddour-Hadjean, R., Franger, S., Bach, S., and Pereira-Ramos, J.P. (2003). Raman spectra of birnessite manganese dioxides. Solid State Ion 159, 345–356. https://doi.org/10.1016/S0167-2738(03)00035-3.
- Ressler, T., Brock, S.L., Wong, J., and Suib, S.L. (1999). Multiple-scattering EXAFS analysis of tetraalkylammonium manganese oxide colloids. J. Phys. Chem. B 103, 6407–6420. https:// doi.org/10.1021/jp9835972.
- 59. Banerjee, D., and Nesbitt, H.W. (1999). XPS study of reductive dissolution of

- birnessite by oxalate: rates and mechanistic aspects of dissolution and redox processes. Geochim. Cosmochim. Acta 63, 3025–3038. https://doi.org/10.1016/s0016-7037(99)00230-6.
- Biesinger, M.C., Payne, B.P., Grosvenor, A.P., Lau, L.W., Gerson, A.R., and Smart, R.S. (2011). Resolving surface chemical states in XPS analysis of first row transition metals, oxides and hydroxides: Cr, Mn, Fe, Co and Ni. Appl. Surf. Sci. 257, 2717–2730. https://doi.org/10. 1016/j.apsusc.2010.10.051.
- Cornell, R.M., and Giovanoli, R. (1988). Transformation of hausmannite into birnessite in alkaline media. Clays Clay Miner 36, 249–257. https://doi.org/10.1346/ccmn. 1988.0360306.
- 62. Tan, Z., Sato, K., and Ohara, S. (2015). Synthesis of layered nanostructured TiO<sub>2</sub> by hydrothermal method. Adv. Powder Technol. 26, 296–302. https://doi.org/10.1016/j.apt.2014. 10.011.
- Ren, G., Sun, M., Sun, Y., Li, Y., Wang, C., Lu, A., and Ding, H. (2017). A cost-effective birnessitesilicon solar cell hybrid system with enhanced performance for dye decolorization. RSC advances 7, 47975–47982. https://doi.org/10. 1039/c7ra08468d.
- 64. Kitchaev, D.A., Peng, H., Liu, Y., Sun, J., Perdew, J.P., and Ceder, G. (2016). Energetics of MnO<sub>2</sub> polymorphs in density functional theory. Phys. Rev. B 93, 045132. https://doi.org/ 10.1103/physrevb.93.045132.
- Ma, S., Ye, X., Jiang, X., Cen, W., Jiang, W., and Wang, H. (2021). First principles calculation of mechanical, dynamical and thermodynamic properties of MnO2 with four crystal phases. J. Alloys Compd. 852, 157007. https://doi.org/ 10.1016/j.jallcom.2020.157007.
- Sun, J., Ruzsinszky, A., and Perdew, J.P. (2015). Strongly constrained and appropriately normed semilocal density functional. Phys. Rev. Lett. 115, 036402. https://doi.org/10.1103/ physrevlett.115.036402.
- 67. Kitchaev, D.A., Dacek, S.T., Sun, W., and Ceder, G. (2017). Thermodynamics of phase selection in MnO<sub>2</sub> framework structures through alkali intercalation and hydration. J. Am. Chem. Soc. 139, 2672–2681. https://doi.org/10.1021/jacs. 4b11301
- Young, M.J., Neuber, M., Cavanagh, A.C., Sun, H., Musgrave, C.B., and George, S.M. (2015). Sodium charge storage in thin films of MnO<sub>2</sub> derived by electrochemical oxidation of MnO atomic layer deposition films. J. Electrochem. Soc. 162, A2753–A2761. https://doi.org/10. 1149/2.0671514jes.
- Al-Falahi, A.H. (2013). Structural and optical properties of MnO<sub>2</sub>: Pb nanocrystalline thin films deposited by chemical spray pyrolysis. OSRG J. of Eng. 3, 52–57. https://doi.org/10.9790/3021-03445257.
- Wang, L., Takada, K., Kajiyama, A., Onoda, M., Michiue, Y., Zhang, Watanabe, M., and Sasaki, T. (2003). Synthesis of a Li-Mn-oxide with disordered layer stacking through flocculation of exfoliated MnO<sub>2</sub> nanosheets, and its electrochemical properties. Chem. Mater. 15,



- 4508–4514. https://doi.org/10.1021/cm0217809.
- 71. Luo, J., Zhang, Q., and Suib, S.L. (2000). Mechanistic and kinetic Studies of crystallization of birnessite. Inorg. Chem. 39, 741–747. https://doi.org/10.1021/ic9904561.
- Zhang, A., Zhao, R., Hu, L., Yang, R., Yao, S., Wang, S., Yang, Z., and Yan, Y. (2021). Adjusting the coordination environment of Mn enhances supercapacitor performance of MnO<sub>2</sub>. Adv. Energy Mater. 11, 2101412. https:// doi.org/10.1002/aenm.202101412.
- 73. Yang, D.S., and Wang, M.K. (2001). Syntheses and characterization of well-crystallized

- birnessite. Chem. Mater. 13, 2589–2594. https://doi.org/10.1021/cm010010e.
- Oaki, Y., and Imai, H. (2007). One-pot synthesis of manganese oxide nanosheets in aqueous solution: chelation-mediated parallel control of reaction and morphology. Angew. Chem. Int. Ed. 46, 4951–4955. https://doi.org/10.1002/ anie.200700244.
- Thompson, K., Lawrence, D., Larson, D., Olson, J., Kelly, T., and Gorman, B. (2007). In situ site-specific specimen preparation for atom probe tomography. Ultramicroscopy 107, 131–139. https://doi.org/10.1016/j.ultramic. 2006.06.008.
- Kresse, G., and Furthmüller, J. (1996). Efficient iterative schemes for ab initio total-energy calculations using a plane-wave basis set. Phys. Rev. B 54, 11169–11186. https://doi.org/10. 1103/PhysRevB.54.11169.
- Blöchl, P.E. (1994). Projector augmented-wave method. Phys. Rev. B 50, 17953–17979. https://doi.org/10.1103/physrevb.50.17953.
- Zheng, W., Halim, J., Yang, L., Badr, H.O., Sun, Z., Persson, P.O.A., et al. (2022). MXene//MnO<sub>2</sub> Asymmetric Supercapacitors with High Voltages and High Energy Densities. Batteries & Supercaps, In press. https://doi.org/10.1002/ batt.202200151.